Cation Influence on Carrier Dynamics in Perovskite Solar Cells

Ankur Solanki[1], Pankaj Yadav[2], Silver-Hamill Turren-Cruz[3], Swee Sien Lim[1],Michael Saliba[3] and Tze Chien Sum[1,]*

Dr. Ankur Solanki, Dr.Swee Sien Lim,and Prof. Tze Chien Sum*

Division of Physics and Applied Physics, School of Physical and Mathematical Sciences, Nanyang Technological University, 21 Nanyang Link, Singapore 637371, Singapore

*Email: Tzechien@ntu.edu.sg

Dr. Pankaj Yadav

Department of Solar Energy, Pandit Deendayal Petroleum University, Gandhinagar-380007, India

Dr. Silver-Hamill Turren-Cruz and Dr. Michael Saliba

Adolphe Merkle Institute, Chemins des Verdiers 4, CH-1700 Fribourg

Keywords: Perovskite solar cell, rubidium, cesium, charge carrier dynamics, recombination.

Abstract: Rubidium and Cesium cations (Rb^+ and Cs^+) incorporation recently emerged as a viable strategy to enhance perovskite solar cells (PSCs) efficiency. However, a clear understanding of the impact of these cations on the structure-function relationship in relation to the device performance is severely lacking. Here, we systematically investigate the influence of Rb^+ and Cs^+ on the carrier dynamics using transient optical spectroscopy and correlate with solar cell performance. Unlike Rb^+, Cs^+ integrates well with methylammonium (MA^+) and formamidinium (FA^+) yielding increased perovskite grain size, longer charge carrier lifetimes and improved power conversion efficiency (PCE). Concomitant incorporation of Cs^+/Rb^+ cooperatively retards radiative recombination by ~60% in the quaternary-cation based perovskite system (RbCsMAFA) compared to the dual-cation MAFA samples. By suppressing the defect density, PCEs around 20% are obtained along with more balanced charge carrier diffusion length and comparable photoluminescence quantum yield in quaternary-cation perovskites. While the synergistic addition of Rb^+ and Cs^+ is attractive for controlling defects and recombination losses in efficient solar cells development, sole incorporation of Rb^+ is still an engineering challenge. Importantly, our study explicates the underlying mechanisms behind the synergistic combination of cations to minimize the charge carrier losses and achieve high efficiency perovskite solar cells.

1. Introduction

In past few years, hybrid metal halide perovskite solar cells (PSCs) have captured considerable attention due to their substantial gains in power conversion efficiency (PCE) from 3.8% in 2009 to the current state-of-the-art of over 23.2%[1]. The outstanding optoelectronic features, high absorption coefficient[2], tunable band edges, low trap density[3], long charge-carrier diffusion length with long lifetimes[4], low exciton binding energy[5] and excellent transport properties

have contributed to their impressive performance. Moreover, their compatibility with facile fabrication techniques, like spin coating[6], sequential-step inter-diffusion[7], thermal evaporation[8], atomic layer deposition[9], and chemical vapour deposition[10] make PSCs attractive candidates for low-cost, renewable energy. To date, the highest efficiencies obtained are from lead-based perovskite with the general formula ABX_3: where A represents a single cation or a mix of different cations (methylammonium ($CH_3NH_3^+$, MA^+) and formamidinium ($CH_3(NH_2)_2^+$, FA^+), cesium (Cs^+), etc.); B represents the divalent metal cation (Pb or Sn); while X represents a single halide anion or a mix of different halide anions (I^- and Br^-).[11]

Since the early days of PSC development, methylammonium lead iodide perovskite ($MAPbI_3$) is the most commonly used light harvester with a demonstrated efficiency higher than 20%.[12] However, $MAPbI_3$'s structural phase transition at temperatures above 85 °C and instability under humid environment, air and heat makes it less appealing for industrial applications.[13] Although partial substitution of MA^+ by FA^+ to form mixed or double cation perovskites ($(MA_{0.17}FA_{0.83})Pb(I_{0.83}Br_{0.17})_3$ or MAFA) helps to enhance PCE, instability under humidity and heat stress still remains, possibly due to the volatile nature of MA and the remnant non-reacting impurities.[14-15] From the literature,[16] partial replacement of MAFA by cesium (Cs) to form the triple cation perovskite ($(MAFA)_{0.95}(CsI)_{0.05}$ or CsMAFA) eliminates the remnant non-reacting impurities; resulting in solar cells with efficiencies exceeding 21% with excellent long term stability under continuous light exposure. In a recent work, the Goldschmidt tolerance factor based on the ionic radius of organic cations using rubidium (Rb^+) as the fourth cation was finetuned and Rb-modified CsMAFA (or $(MAFA)_{0.95}(RbI)_{0.05}$) was developed as a new family of perovskites.[17-18] By varying the fraction of different cations, the composition $Rb_5(Cs_5MAFA)_{95}$ yielded a record open circuit voltage of 1.24 V with 21.6% efficiency. This work also demonstrates the first high stability cells operating at elevated temperatures of 85 °C under 500 hours of continuous illumination.

Analogously, other inorganic cations *i.e.*, potassium (K^+), sodium (Na^+) and lithium (Li^+) also demonstrate their potential to stabilize the double perovskite and enhance the PCE.[19] Jalebi *et al.* incorporated K^+ in CsMAFA to mitigate the non-radiative recombination and photoinduced ion migration by passivating the defects on surface and grain boundaries.[20] The suppressed losses in perovskite films results in films with 66% photoluminescence quantum yield and in solar cells with efficiency more than 21%. Furthermore, Cao *et al.* conducted density functional theory (DFT) calculations and demonstrate that the interstitial occupancy by inorganic cations is energetically favourable to enhance the ion migration energy barrier in the lattice.[21] Despite such extensive research on the optoelectronic and structural properties of these multi-cation systems[22-28], a clear understanding of the role of organic and inorganic cations, *i.e.*, MA^+, FA^+, Cs^+ and Rb^+, on the photophysical process and their relationship with photovoltaic performance is still lacking. Recently, Hu *et al.* investigated the PCE performance of planar perovskite devices with different cations and correlated with the charge transport properties measured using different electrical probing techniques.[29] An in-depth study of the structural properties correlated with the photophysical properties (*e.g.*, charge carrier dynamics, recombination rates, diffusion lengths and photoluminescence quantum yield (PLQY)) will provide a complementary perspective to better understand the loss mechanisms needed for the development of efficient PSCs.

Herein, steady-state and time-resolved photoluminescence techniques were used to investigate the roles of different cations on the charge carrier trap-density and their influence on the recombination lifetimes and diffusion lengths in MAFA, RbMAFA, CsMAFA and RbCsMAFA cations-based perovskite films. Throughout this study, the double cation MAFA perovskite composed of MA^+ and FA^+ as the reference sample. The triple cation-based perovskites CsMAFA and RbMAFA were obtained by mixing 5% of Cs^+ and 5% Rb^+ in MAFA reference perovskite, respectively. The final and fourth quadruple cation perovskite

RbCsMAFA was prepared by mixing Rb^+ and Cs^+ concurrently in MAFA perovskite as described in experimental section. The relatively higher trap-density ($15 \pm 3.0 \times 10^{17}$ cm^{-3}) and thus stronger trap-assisted monomolecular recombination in RbMAFA perovskite film results in a lower fill factor in these solar cells. We attribute this to a larger presence of remnant species and non-perovskite phase amongst the four perovskite films. The incorporation of Cs^+ into MAFA passivates the trapping sites in CsMAFA perovskite. This results in lower trap densities and longer charge carrier lifetimes; which are consistent with the higher PCE. Interestingly, with the simultaneous addition of Rb^+ and Cs^+ in RbCsMAFA perovskite, there is a significant reduction of trap-related losses as reflected by the lowest monomolecular recombination rate ($4.1 \pm 0.6 \times 10^{-6}$ cm^{-1}) and reduced trap density amongst these perovskites. Consequently, the prolonged carrier lifetimes and more balanced carrier diffusion lengths in these films give rise to devices with the highest fill factor and PCE amongst the four perovskite films.

2. Results

2.1. Photovoltaic performance and thin film properties

Cations concentration in perovskites are well-known to exert a strong influence over the solar cell device efficiency. The perovskite composition with 5% of CsI and RbI (each) are reported in the literature to exhibit the best device efficiency and stability in mixed perovskites. We have therefore used this composition here to investigate the influence of inorganic cations on the charge carrier dynamics in perovskite films. **Figure 1a** represents the schematic diagram of different cation based planer solar cell devices. The current-voltage (*J*-*V*) characteristics of devices measured under Air Mass (AM) 1.5 illumination fabricated with MAFA, RbMAFA, CsMAFAand RbCsMAFA perovskite films are depicted in **Figure 1b**. The extracted corresponding photovoltaic parameters are summarized in Table 1 and the statistical PCE

performance based on 25 planar devices is shown in **Figure S1**. Solar cell devices with quadruple cation RbCsMAFA perovskite show the typical PCE of 19.1% (short-circuit current density J_{SC} = 22.4 mA-cm^{-2}, open circuit voltage V_{OC} = 1.17 V and fill factor *FF* = 73%), compared to PCE = 16.5% of double cation MAFA and triple cation perovskites RbMAFA (PCE = 17.1%)/CsMAFA (PCE = 17.9%). The complete device fabrication process is described in the experimental section.[17, 22] State-of-the-art solar cells in meso-device configuration were also prepared for comparison which confirm the similar PCE trend regardless of the device structure (**Table S1**). **Figure S2** depicts the scanning electron microscopy (SEM) topography images of different perovskite films. The small grains with the presence of other smaller bright grains in MAFA perovskite (**Figure S2 (a)**) is assigned to an excess of lead iodide as described in the Materials and Methods section.[30] The incorporation of Cs^+ as the third cation in MAFA results in an increased perovskite grain size; signifying improved crystallinity with better surface coverage (**Figure S2 (c)**). A similar effect on grain sizes is observed with the incorporation of Rb in MAFA (**Figure S2 (b)**), though smaller grains surrounded by larger grains are still observed which can be assigned as remnant PbI_2[30] or Rb/Br-rich orthogonal phases segregated from the perovskite phase. Further incorporation of Rb^+ as the fourth cation in CsMAFA perovskite reduces the grains dimension with some distorted structure as (**Figure S2(d)**), although the grain sizes are still larger than that of MAFA perovskite film. **Figure S3** shows the UV-vis absorption and PL spectra of these perovskite films coated on glass substrates.

To gain further insights into the role of organic and inorganic cations, *i.e.*, MA^+, FA^+, Cs^+ and Rb^+ on the device performance, we estimated the charge carrier trap density in these perovskite film (coated on transparent glass substrates). Excitation intensity-dependent steady-state

photoluminescence measurements were performed with an excitation wavelength of 600 nm in the low fluence regime (~0.22 - 16 μJ-cm^{-2}), where Auger recombination is negligible. To prevent ambient exposure during the experiment, all the samples were sealed in a quartz window holder with N_2 environment for spectroscopic measurements. **Figure 2a** shows a plot of excitation carrier density vs integrated PL intensity for different films and fitted with the model:[31]

$$n_c(0) = \sum n_{TP}(0)(1 - e^{-k_1 I_{PL}}) + k_2 I_{PL}$$

where $\boldsymbol{n_c(0)}$ and $\boldsymbol{n_{TP}}$ represent photogenerated charge carrier density and trap density, respectively while k_1, k_2 are the constants (See SI for the method). In this model, the infinite number of charge trapping pathways are considered the origin of the trap density states influencing the trapping rate within the perovskite films. Based on the fit, the trap density in MAFA perovskites was estimated to be 7.4 x 10^{17} cm^3 - consistent with previously reported values for three-dimensional perovskites.[31] Generally, voids, grain boundaries, external impurities etc. are the source of traps in perovskite film and are strongly dependent on the processing methodology. A higher trap density of 15.0 × 10^{17} cm^3 was observed in RbMAFA thin films. XRD measurements were conducted on these thin films (**Figure S4**) in a bid to establish the origins of the trapping centers. An XRD peak at 2θ = 10.16° was observed, indicating the formation of orthorhombic, non-perovskite Rb-rich[32] phase associated with other I^-/Br^- rich phases acting as trapping centers.[33] Cao *et al.* also observed Rb-rich phases in Rb^+ incorporated perovskite thin films.[21] On the other hand, the incorporation of Cs^+ in MAFA perovskite suppresses the trap density to 6.7 x 10^{17} cm^3 (CsMAFA perovskite), without any detectable presence of the undesired phase. In contrast to the independent addition, the concomitant incorporation of Cs^+ and Rb^+ cations in MAFA perovskite to form RbCsMAFA appears more effective as shown in **Figure 2a**. The presence of Cs^+ in MAFA helps with better

Rb^+ incorporation, which in turn passivates the traps in MAFA perovskite more effectively. This reduces the trap density to less than half (3.5×10^{17} cm^3). These findings agree well with the findings of previous reports.[17, 22] The higher PCE and fill factor in CsMAFA and RbCsMAFA -based perovskite film are consistent with a lower trap density compared to MAFA and RbMAFA based perovskite solar cells.

2.2 Impact on the Carrier Dynamics and Recombination.

The carrier dynamics in these perovskite thin films were further examined using time-resolved photoluminescence (TRPL) spectroscopy. A low fluence of ~0.22 μJ-cm^{-2} at the pump wavelength of 600 nm was used to excite the films (**Figure 2b**). Under such low fluence excitation, multiple particle interactions which influence the PL lifetime, can be avoided. PL kinetics for all perovskite films were fitted mono-exponentially with the fitting value as R^2 ~ 0.99. For the MAFA film, the photo-excited charge carriers exhibit an approximate PL lifetime of 240 ± 10 ns. Upon Cs^+ incorporation, the PL lifetimes lengthened slightly to around 290 ± 20 ns in the CsMAFA films. Further PL lifetime lengthening to 360 ± 20 ns is achieved upon Rb^+ addition in RbCsMAFA perovskite films. These results suggest that the traps in MAFA are suppressed by Cs^+ incorporation; and can be further suppressed by Rb^+ incorporation. Our findings of PL lifetimes are in good agreement with Jacobsson *et al.* where the presence of Rb^+ with Cs^+ suppress the recombination losses significantly.[19] This is also consistent with the enlargement of the perovskite grain size in RbCsMAFA perovskite as shown in SEM topographical images (**Figure S2**) and the results of reduced trap density in the previous section.[22] However, with Rb^+ incorporation alone, *i.e.*, RbMAFA, the converse occurs with increased trap density and shorter PL lifetime of 175 ± 9 ns.

Based on the steady-state and transient measurements, we conclude that the presence of Cs^+ influences the integration of Rb^+ in MAFA perovskite and redefines the charge transport and recombination properties in the resulting thin films. On the other hand, the existence of higher defect density in RbMAFA perovskite film can be understood from the distortion of the perovskite crystal structure. Empirically, the cationic radius determines the formation of perovskite lattice structure. In the case of smaller ionic radius of Rb (~152 pm), the tolerance factors of $RbPbI_3$ and $RbPbBr_3$ are smaller than 0.8, which is below the formation regime of black phase perovskite and can be a source of the trapping centers.[34-35] On the other hand, Cs^+ with an ionic radius (~167 pm) compared to MA^+ (~217 pm) and FA^+ (~253 pm) have a perovskite lattice structure with a tolerance factor between 0.8 and 1.0.[17, 36] Furthermore, $RbPbI_3$ does not have a phase transition at higher temperatures unlike $CsPbI_3$, hence the interaction of halides with these two cations is also different and could be an origin of the defects affecting the charge carrier dynamics.[33]

To quantitatively evaluate the recombination rates, pump fluence dependent dynamics of fabricated perovskite films were measured and globally-fitted with the rate equation: $dn/dt = -k_1 n - k_2 n^2 - k_3 n^3$. This is shown in **Figure S5**, where k_1, k_2 and k_3 are the monomolecular, bimolecular and Auger recombination rate constants, respectively, while *n* represents the charge carrier density.Here, k_1 also accounts for the trap-mediated recombinations in these perovskite films. The extracted fitting parameters are summarized in **Table 2** and graphically represented in **Figure 3(a)**. The monomolecular recombination rate constant is obtained either by the annihilation of spatially bound conduction band electron and valence band hole, or by bound electron-hole pair (exciton) annihilation. Owing to the low exciton binding energy (<25 meV)[37-38] in hybrid perovskites at room temperature, the

predominant species are free charge carriers instead of excitons. A second process bimolecular recombination, which occurs at higher fluence, involves the radiative annihilation of free electrons and holes. The third process is Auger recombination that involves multiple particle interactions and is, therefore, strongly excitation intensity dependent. In this study, the fluence dependent dynamics were well-fitted by considering the first two processes.

In the standard MAFA system, the monomolecular recombination constant k_1 is estimated to be 10×10^{-6} s^{-1}, which is relatively low for 3D perovskites in efficient solar cells.[39] The rate constant k_1 obtained for perovskite films is mainly from trap-assisted recombination: *i.e.*, defects such as pinholes, grain boundaries, impurities, non-perovskite phase, etc.[40] Furthermore, Philippe, B. *et al.* recently found that the un-reacted organic cation (FAI) and halides (PbI_2, Br^-/I^-) are the main remnant species in MAFA perovskite films.[22] The presence of such sites in perovskites act as charge trapping centers and leads to trap-assisted charge carrier recombination. The incorporation of Rb^+ and Cs^+ as a third cation could possibly react with these un-reacted species in MAFA and transform them into the perovskite phase as confirmed from XRD (**Figure S4**) and previous reports.[17] However, our analysis shows higher values of the monomolecular rate constant in the triple cation systems (41×10^{-6} s^{-1} in RbMAFA, and 24×10^{-6} s^{-1} in CsMAFA) compared to the double cation system (10×10^{-6} s^{-1} in MAFA). The larger grain size in RbMAFA and CsMAFA compared to MAFA, as observed in SEM (**Figure S2**), indicates that non-perovskite phase, remnant species and defects that are present inside the perovskite grains, are the predominant recombination centers[22].

The relatively lower monomolecular recombination rate constant in CsMAFA compared to RbMAFA is consistent with the findings from the trap density - indicating that Cs^+ incorporate

into MAFA easily and result in better thin film quality compared to the sole addition of Rb^+. It is noteworthy that all the photo-physical investigations are conducted on thin films without any external field where charge carrier transport is only diffusion-limited. In case of solar cell devices, the presence of the electrode generates an external field on the charge carriers which drift them towards the respective electrodes. Based on the field magnitude and mobility, there is the possibility to bypass the recombination processes if charge carriers are efficiently collected on the electrodes. Correlating with the performance of RbMAFA based solar cells, charge transport as well as charge collection in these devices appears sufficient to extract them before recombination occurs inside the active layer. However, without any extraction layers, the charges annihilate more efficiently, resulting in strong trap-assisted recombination and hence shorter lifetimes. On the other hand, the concomitant incorporation of Cs^+ and Rb^+ in MAFA decreases the monomolecular rate constant by ~60 % with 4.1×10^{-6} s^{-1} in RbCsMAFA compared to MAFA (10.0×10^{-6}). This is consistent with the reduced trap density owing to the better incorporation of Rb^+ in the presence of Cs^+ which results in efficient charge transport properties. The charge carrier recombination in thin films is also directly correlated with the series resistance and the fill factor trends in solar cells.[41] The higher recombination in MAFA thin films results a highest series resistance (9 ohm-cm^2) to yield a lower fill factor **(Table 1)**. On the other hand, the reduced recombination in RbCsMAFA perovskite accounts for the lower series resistance (5 ohm-cm^2) and increase of the fill factor to 73% - most likely due to minimal remnant impurities.

Carrier diffusion length is another important parameter to assess the impact of different cations on charge transport kinetics in perovskite films. To estimate the electron and hole diffusion length, a thin layer of PCBM (([6,6]-Phenyl C_{61} butyric acid methyl ester) and spiro-OMeTAD

on top of the perovskite layers was spin-coated as electron and hole quenching material, respectively. The low pump fluence (~0.5 μJ-cm^{-2}) kinetics for different perovskite and perovskite/PCBM films were fitted with a mono-exponential function while the kinetics for perovskites/spiro-OMeTAD were fitted with a bi-exponential function (**Figure S6**). To estimate the charge carrier diffusion length, a one-dimensional diffusion length model was used:[4]

$$\frac{L_D}{L} = \frac{2}{\pi}\sqrt{(\frac{1}{\tau_D/\tau_0} - 1)}$$

, where L_D and L are the diffusion length and film thickness while τ_D and τ_0 represents fitting lifetimes with and without quenching layer, respectively. For the calculation, the thickness for all perovskite films is taken to be L = 400 nm. The obtained diffusion lengths are summarized in **Table 2** and graphically presented in **Figure 3b**. The electron diffusion length in MAFA perovskite drops from 510 nm to 330 nm in RbFAMA perovskite. A lower electron diffusion length may be due to higher trap-assisted recombination, consistent with the above discussion in the context of **Figure 2a**. A more balanced and longer charge carrier diffusion length (d_e = 600 nm and to d_h = 460 nm) in RbCsMAFA films is very likely due to increased charge carrier mobility[42] in larger perovskite crystals and decreased defect density. Based on the significant improvements of electron diffusion lengths in CsMAFA (d_e = 610 nm) and RbCsMAFA (d_e = 600 nm)), we propose that the trapping sites in MAFA are predominantly electrons trapping sites that are mostly passivated by Cs.

For trap-mediated non-radiative recombination, the trapped carriers are unable to recombine through band-to-band transitions and thus charge trapping dominate the PL dynamics. Therefore, it is also vital to relate with photoluminescence quantum yield (PLQY) before establishing any correlation between the photovoltaic parameters with carrier lifetime and

recombination rates. PLQY estimates the ratio of the radiatively recombined charge carriers to the total population of optically excited charge carriers. It has a direct impact on the photovoltaic parameters of a working solar cell device, which is limited by the occurrence of the trap-assisted radiative recombination in the film.[43] The lower PLQY values obtained from CsMAFA (3.4%) compared to MAFA (5.3%) perovskite indicates a reduced trap-assisted radiative recombination loss in the former, which in turn increase the collection of the charges at the electrode in devices and hence the higher FF (72%) (**Figure 4)**. Furthermore, the inverse relationship of V_{OC} with PLQY of our samples is also well-described by the equation, $eV_{oc} = E_g - kTln(PLQY)$ (where, E_g is the bandgap to perovskite and kT represents the room temperature energy) among all these perovskites films (**Figure 4**).[44] The highest PCE achieved with efficient charge transport in RbCsMAFA (PLQY = 4.6%) is attributed to the reduced non-radiative recombination from trap states passivation following Rb^+ addition as the fourth cation as indicated by highest V_{OC} (1.17 V). The higher trap-assisted radiative recombination in RbMAFA perovskite-based solar cell devices corresponds to the higher PLQY value (8.3%) along with the rise in V_{OC}. Thus, the presence of Rb^+ either suppresses the non-radiative states or enhances the radiative pathways. Generally, defects in perovskite films are dominated by interstitial and anti-site defects, which are deep-level defects and leads to non-radiative trap-assisted recombination.[45] As reported previously, the rise in EQE at a driving current higher than J_{SC} also suggests that Rb^+ help to mitigate the dominating non-radiative recombination centers and enhance the performance.[17] The PLQY measurements are also consistent with solar cell performance and charge carrier dynamics obtained from transient measurements.

2.3. Discussion

Our in-depth analysis on the carrier dynamics reveal that the addition of Cs^+ in double perovskite system reduces the trap density and extend the electron and hole diffusion lengths significantly.[42] However, these devices with their excellent characteristics still suffer from the lower V_{OC} as compared to MAFA based devices. In solar cell devices, V_{OC} is not only determined by recombination, but also depends on charge accumulation. Here, we propose that the accumulation of photogenerated charges in MAFA devices manifests in the high open circuit voltage; while the higher barrier for accumulation of charges in CsMAFA leads to the lower V_{OC}.[46] Further in-depth study on capacitance versus frequency responses is required to reveal the mechanism. On the other hand, the relatively short charge carrier lifetime and diffusion lengths in RbMAFA film are compensated by improved charge extraction under the influence of external electric field in devices which results in higher J_{SC}. The higher charge carrier mobility or improvement of the ETL/perovskite or perovskite/HTL interfaces by the suppression of charge accumulation and thus reduced interfacial recombination in the presence of Rb^+ could be the probable reasons behind the efficient charge extraction.[42, 47] The higher defect density present in the film causes trap-assisted radiative recombination. Based on the charge dynamics and optoelectronics properties we infer that non-radiative losses are dominant in CsMAFA while charge carriers are mainly lost radiatively in RbMAFA perovskite film. The unique respective advantages of Cs^+ and Rb^+ are synergistically combined in RbCsMAFA perovskite, which leads to minimal defect density, increased PL lifetime, extended charge carrier diffusion lengths and moderate PLQY. Furthermore, we hypothesize that the incorporation of Rb^+ contributes differently across the bulk and interfaces. The presence of Rb^+ at the interface in RbCsMAFA strongly suppresses the charge accumulation and reduces the surface recombination as compared to CsMAFA which enhances the potential difference across the device for higher V_{OC}. This is in excellent agreement with some of the recent works

where .[19, 29, 48] On the other hand, the presence of Rb^+ inside the bulk in association with Cs^+ passivates the physical defects and suppress the non-perovskite phase, which gives the efficient charge transport properties in RbCsMAFA perovskite. This in turn cooperatively yields a high V_{OC} (due to reduced non-radiative recombination), high FF (due to improved charge extraction), and suppresses ionic motion, resulting in higher PCE solar cell devices. The extensive structural characterizations by Jacobsson *et al.* confirms good integration of Cs^+ with MAFA to passivate the defects and suppress the recombinaton losses (as compared to Rb^+); while the longer fluorescence lifetime in RbCsMAFA samples is assumed to be the dominating factor for the efficiency improvement.[19]

The schematic in **Figure 5** summaries the influence of different cations on morphology and defects density in perovskite films along with the representation of charge carrier diffusion lengths. The smaller perovskite grain size and higher defect density in MAFA system leads to a higher charge carrier recombination rate and hence unbalanced diffusion length. Thus, incorporation of different cations can be used to tune the structural-functional relations and specifically, the synergistic co-existence of Cs^+/Rb^+ in quaternary cation perovskites unlocks unique advantages for perovskite solar cells.

3. Conclusions

Here, we have systematically investigated the effects of different cations (MA^+, FA^+, Cs^+ and Rb^+) on the charge carrier dynamics in perovskite thin films and correlated these with solar cell device performance. Our study suggests that the incorporation of Cs^+ to form CsMAFA perovskite suppresses the defect density, leading to longer charge carrier lifetimes, lower PLQY and higher power conversion efficiencies compared to double cation perovskite. In contrast, the addition of Rb^+ leads to a higher defect density, causing a drop-in charge carrier lifetime and

increase in trap-assisted radiative recombination – attributed to the formation of undesired non-perovskite phases. However, the improved PCE is expected from the efficient charge extraction before charge recombination in solar cell devices. The synergistic incoporation of both Rb^+ and Cs^+ in RbCsMAFA perovskite-based solar cells leads to prolonged charge carrier lifetimes with balanced diffusion lengths and reduced defect densities. Our study aptly highlights the importance of a judicious selection of the organic/inorganic cations to suppress the charge carrier trapping centers and trap-assisted monomolecular recombination loss as the route to high efficiency perovskite solar cells.

4. Experimental details

Substrate and perovskite solution preparation: To make the perovskite solar cells in configuration of FTO/compact-TiO_2/perovskite/spiro-OMeTAD/Au, substrates were prepared as follows:

FTO glass substrates were cleaned through sonication in 2% Hellmanex water solution. Substrates were further cleaned thoroughly by DI-water before conducting plasma treatment of the FTO surface for 15 min. To prepare the compact TiO_2 layer, a precursor solution prepared by mixing titanium diisopropoxide bis(acetylacetonate)in anhydrous ethanol was deposited on FTO by spray pyrolysis at 450 °C to achieve a thin compact TiO_2 layer and subsequently cool down to room temperature after heating for 45 min at the same temperature.

In order to make FTO/compact-TiO_2/Li-doped mesoporous TiO_2/perovskite/spiro-OMeTAD/Au solar cell devices for the comparison, a 150-200 nm thick mesoporous TiO_2 was

achieved by spin coating the Dyesol 30 NR-D paste mixed with ethanol on compact-TiO_2. The annealing process was conducted in two steps with 10 min immediate drying at 100 °C followed by 30 min drying at 450°C with subsequent cooling to room temperature. A 0.1 M Li-TFSI solution diluted in acetonitrile was again spin coated to accomplish the Li-doping of mesoporous TiO_2.

To prepare the different perovskite solutions, all organic cation salts were purchased from Dysole while lead iodide and inorganic salts (CsI and RbI) were bought from TCI and abcr GmbH, respectively. Preparation details for different perovskite composition is as follows:

MAFA perovskite solution: The "mixed" or double cation perovskite precursor solution was prepared by mixing FAI (1 M), PbI_2(1.1 M), MABr (0.2 M), and $PbBr_2$ (0.22 M) in anhydrous DMF:DMSO (4:1 by volume). Note that a nonstoichiometric solution based on the previous reports was prepared using the excess 10 mole % of the lead precursors achieve the formulation $(MA_{0.17}FA_{0.83})Pb(I_{0.83}Br_{0.17})_3$, 0.1[0.83$PbI_2$, 0.17$PbBr_2$], referred as MAFA.

CsMAFA perovskite solution was prepared by adding 5% (by vol) pre-dissolved CsI salt in DMSO (1.5M) in double perovskite MAFA solution. The resultant solution was labelled as CsMAFA or triple cation perovskite with the composition of $(MAFA)_{0.95}(CsI)_{0.05.}$

A similar procedure to CsMAFA was used to prepare RbMAFA perovskite solution except RbI (1.5M) was used to predissovle in DMF/DMSO 4:1 (by vol) instead of CsI in DMSO. The

resultant solution was labelled as RbMAFA perovskite solution with the formulation $(MAFA)_{0.95}(RbI)_{0.05.}$

Finally, quadruple cation perovskite solution was prepared by adding of 5% of 1.5M RbI stock solution into CsMAFA solution to achieve the composition $(MAFA)_{0.9025}(CsI)_{0.0475}(RbI)_{0.05.}$ The final solution was labelled as RbCsMAFA perovskite solution.

Perovskite solar cell device fabrication and characterization: Different perovskite solution were deposited on pre-prepared FTO glass substrates by one-step spin coating using a two-step spin recipe of 1000 rpm for 10s and then 6000 rpm for 30s. The anti-solvent treatment was performed by dripping 100 µl chlorobenzene on the spinning substrate 10s prior to the end of spinning. To conduct the XRD and optical measurements, different perovskite films were prepared on glass substrates. Subsequently, all perovskite films were thermally annealed at 100 for 60 min. A spiro-OMeTAD film as hole conductor on perovskite layer was prepared as reported previously.[16] Finally, ~80 nm gold (Au) electrode on thin films was thermally deposited under high vacuum through a shadow mask. The *J-V* characteristics of perovskite solar cell devices were measured using Keithely 2400 source meter. Devices were illuminated by 450 W xenon lamp (Oriel, USA) to obtain the light characteristics.

Film preparation for Transient measurements: To measure the low fluence lifetime, MAFA, CsMAFA, RbMAFA and RbCsMAFA perovskite films using the same processing parameters were prepared on cleaned transparent glass substrates. To measure the hole diffusion length, a spiro-OMeTAD hole quenching layer was spin-coated at 4000 rpm for 30s. On the other hand,

PCBM ([6,6]-Phenyl C_{61} butyric acid methyl ester purchased from nano-C) pre-dissolved in cholorobenzene (20 mg/ml) was spin-coated at 1200 rpm for 45s on perovskite films as the electron quenching layer.

Thin film Characterization: A Bruker-AXS (D8 Advance) X-ray diffractometer equipped with Cu Kα (λ = 1.5418 Å) X-ray source was used to collect the X-ray diffraction pattern. The topography of the perovskite films was obtained using Field Emission Scanning electron microscopy (SEM) (JEOL JSM6700F). A UV-Vis absorption spectra of perovskite films were collected by UV–VIS–NIR spectrophotometer (Shimadzu UV-3600). Steady-state photoluminescence of the perovskite films measured with excitation of 600 nm pump wavelength. The excitation pump was generated from a Coherent OPerA Solo optical parametric amplifier pumped with a Coherent Libra™ regenerative amplifier (50 fs, 1KHz, 800 nm). Steady-state PL was collected on an Acton Spectra Pro 2500i spectrometer coupled with a Princeton Instruments PIXIS 400B CCD camera. An Optronis Optoscope streak camera with temporal resolution of 10 ps was employed to collect the Time-resolved photoluminescence (TRPL). A 473 nm CW laser source was used to excite the samples in integrating sphere and emitted light was collected at Acton Spectra Pro 2500i spectrometer**.**

Acknowledgments:

Financial support from Nanyang Technological University SUG - M4080514 and JSPS-NTU Joint Research Project M4082176; the Ministry of Education AcRF Tier 1 grant RG173/16 and Tier 2 grants MOE2015-T2-2-015 and MOE2016-T2-1-034; and from the Singapore National Research Foundation through the Competitive Research Programme NRF-CRP14-2014-03 and the NRF Investigatorship Programme NRF-NRFI-2018-04 are gratefully acknowledged.

References

[1] N. J. Jeon; H. Na; E. H. Jung; T.-Y. Yang; Y. G. Lee; G. Kim; H.-W. Shin; S. Il Seok; J. Lee; J. Seo, Nat. Energy 3 (2018) 682-689.

[2] G. E. Eperon; S. D. Stranks; C. Menelaou; M. B. Johnston; L. M. Herz; H. J. Snaith, Energ. Environ. Sci. 7 (2014) 982-988.

[3] D. Shi; V. Adinolfi; R. Comin; M. Yuan; E. Alarousu; A. Buin; Y. Chen; S. Hoogland; A. Rothenberger; K. Katsiev; Y. Losovyj; X. Zhang; P. A. Dowben; O. F. Mohammed; E. H. Sargent; O. M. Bakr, Science 347 (2015) 519-522.

[4] G. Xing; N. Mathews; S. Sun; S. S. Lim; Y. M. Lam; M. Graetzel; S. Mhaisalkar; T. C. Sum, Science 342 (2013) 344.

[5] A. Miyata; A. Mitioglu; P. Plochocka; O. Portugall; J. T.-W. Wang; S. D. Stranks; H. J. Snaith; R. J. Nicholas, Nat. Phys. 11 (2015) 582-587.

[6] J. H. Heo; S. H. Im; J. H. Noh; T. N. Mandal; C.-S. Lim; J. A. Chang; Y. H. Lee; H.-j. Kim; A. Sarkar; K. NazeeruddinMd; M. Gratzel; S. I. Seok, Nat. Photon 7 (2013) 486-491.

[7] Z. Xiao; C. Bi; Y. Shao; Q. Dong; Q. Wang; Y. Yuan; C. Wang; Y. Gao; J. Huang, Energ. Environ. Sci. 7 (2014) 2619-2623.

[8] M. Liu; M. B. Johnston; H. J. Snaith, Nature 501 (2013) 395-398.

[9] B. R. Sutherland; S. Hoogland; M. M. Adachi; P. Kanjanaboos; C. T. O. Wong; J. J. McDowell; J. Xu; O. Voznyy; Z. Ning; A. J. Houtepen; E. H. Sargent, Adv. Mater. 27 (2015) 53-58.

[10] Q. Chen; H. Zhou; Z. Hong; S. Luo; H.-S. Duan; H.-H. Wang; Y. Liu; G. Li; Y. Yang, J. Am. Chem. Soc. 136 (2014) 622-625.

[11] M. Saliba; T. Matsui; J.-Y. Seo; K. Domanski; J.-P. Correa-Baena; M. K. Nazeeruddin; S. M. Zakeeruddin; W. Tress; A. Abate; A. Hagfeldt; M. Gratzel, Energ. Environ. Sci. 9 (2016) 1989-1997.

[12] S. S. Shin; E. J. Yeom; W. S. Yang; S. Hur; M. G. Kim; J. Im; J. Seo; J. H. Noh; S. I. Seok, Science 356 (2017) 167-171.

[13] B. Conings; J. Drijkoningen; N. Gauquelin; A. Babayigit; J. D'Haen; L. D'Olieslaeger; A. Ethirajan; J. Verbeeck; J. Manca; E. Mosconi; F. D. Angelis; H.-G. Boyen, Adv. Energ. Mater. 5 (2015) 1500477.

[14] N. J. Jeon; J. H. Noh; W. S. Yang; Y. C. Kim; S. Ryu; J. Seo; S. I. Seok, Nature 517 (2015) 476-480.

[15] N. Pellet; P. Gao; G. Gregori; T.-Y. Yang; M. K. Nazeeruddin; J. Maier; M. Grätzel, Angew. Chem. Int. Edit. 53 (2014) 3151-3157.

[16] M. Saliba; T. Matsui; J.-Y. Seo; K. Domanski; J.-P. Correa-Baena; M. K. Nazeeruddin; S. M. Zakeeruddin; W. Tress; A. Abate; A. Hagfeldt; M. Gratzel, Energ. Environ. Sci. 9 (2016) 1989-1997.

[17] M. Saliba; T. Matsui; K. Domanski; J.-Y. Seo; A. Ummadisingu; S. M. Zakeeruddin; J.-P. Correa-Baena; W. R. Tress; A. Abate; A. Hagfeldt; M. Grätzel, Science 9 (2016) 1989-1997.

[18] S.-H. Turren-Cruz; A. Hagfeldt; M. Saliba, Science 362 (2018) 449-453.

[19] T. J. Jacobsson; S. Svanström; V. Andrei; J. P. H. Rivett; N. Kornienko; B. Philippe; U. B. Cappel; H. Rensmo; F. Deschler; G. Boschloo, J. Phys. Chem. C 122 (2018) 13548-13557.

[20] M. Abdi-Jalebi; Z. Andaji-Garmaroudi; S. Cacovich; C. Stavrakas; B. Philippe; J. M. Richter; M. Alsari; E. P. Booker; E. M. Hutter; A. J. Pearson; S. Lilliu; T. J. Savenije; H. Rensmo; G. Divitini; C. Ducati; R. H. Friend; S. D. Stranks, Nature 555 (2018) 497.

[21] J. Cao; S. X. Tao; P. A. Bobbert; C.-P. Wong; N. Zhao, Adv. Mater. 30 (2018) 1707350.
[22] B. Philippe; M. Saliba; J.-P. Correa-Baena; U. B. Cappel; S.-H. Turren-Cruz; M. Grätzel; A. Hagfeldt; H. Rensmo, Chem. Mater. 29 (2017) 3589-3596.
[23] W. Rehman; D. P. McMeekin; J. B. Patel; R. L. Milot; M. B. Johnston; H. J. Snaith; L. M. Herz, Energ. Environ. Sci. 10 (2017) 361-369.
[24] O. A. Syzgantseva; M. Saliba; M. Grätzel; U. Rothlisberger, J. Phys. Chem. Lett. 8 (2017) 1191-1196.
[25] D. J. Kubicki; D. Prochowicz; A. Hofstetter; S. M. Zakeeruddin; M. Grätzel; L. Emsley, J. Am. Chem. Soc. 139 (2017) 14173-14180.
[26] P. Yadav; M. I. Dar; N. Arora; E. A. Alharbi; F. Giordano; S. M. Zakeeruddin; M. Grätzel, Adv. Mater. 29 (2017) 1701077.
[27] Y. H. Park; I. Jeong; S. Bae; H. J. Son; P. Lee; J. Lee; C.-H. Lee; M. J. Ko, Adv. Funct. Mater. 27 (2017) 1605988.
[28] D. Prochowicz; M. M. Tavakoli; A. Solanki; T. W. Goh; K. Pandey; T. C. Sum; M. Saliba; P. Yadav, J. Mater. Chem. A 6 (2018) 14307-14314.
[29] Y. Hu; E. M. Hutter; P. Rieder; I. Grill; J. Hanisch; M. F. Aygüler; A. G. Hufnagel; M. Handloser; T. Bein; A. Hartschuh; K. Tvingstedt; V. Dyakonov; A. Baumann; T. J. Savenije; M. L. Petrus; P. Docampo, Adv. Energy Mater. 8 (2018) 1703057.
[30] C. Roldan-Carmona; P. Gratia; I. Zimmermann; G. Grancini; P. Gao; M. Graetzel; M. K. Nazeeruddin, Energ. Environ. Sci. 8 (2015) 3550-3556.
[31] G. Xing; N. Mathews; S. S. Lim; N. Yantara; X. Liu; D. Sabba; M. Grätzel; S. Mhaisalkar; T. C. Sum, Nat. Mater. 13 (2014) 476.
[32] I. J. Park; S. Seo; M. A. Park; S. Lee; D. H. Kim; K. Zhu; H. Shin; J. Y. Kim, ACS Appl. Mater. Inter. 9 (2017) 41898-41905.
[33] Y. Hu; M. F. Aygüler; M. L. Petrus; T. Bein; P. Docampo, ACS Energy Lett. 2 (2017) 2212-2218.
[34] G. Kieslich; S. Sun; A. K. Cheetham, Chemical Science 6 (2015) 3430-3433.
[35] M. Cola; V. Massarotti; R. Riccardi; C. Sinistri, Binary Systems Formed by Lead Bromide with (Li, Na, K, Rb, Cs and Tl)Br: A Dta and Diffractometric Study. (1971); 26, 1328.
[36] T. Duong; H. K. Mulmudi; H. Shen; Y. Wu; C. Barugkin; Y. O. Mayon; H. T. Nguyen; D. Macdonald; J. Peng; M. Lockrey; W. Li; Y.-B. Cheng; T. P. White; K. Weber; K. Catchpole, Nano Energy 30 (2016) 330-340.
[37] A. Miyata; A. Mitioglu; P. Plochocka; O. Portugall; J. T.-W. Wang; S. D. Stranks; H. J. Snaith; R. J. Nicholas, Nat. Phys. 11 (2015) 582-587.
[38] K. Galkowski; A. Mitioglu; A. Miyata; P. Plochocka; O. Portugall; G. E. Eperon; J. T.-W. Wang; T. Stergiopoulos; S. D. Stranks; H. J. Snaith; R. J. Nicholas, Energ. Environ. Sci. 9 (2016) 962-970.
[39] M. B. Johnston; L. M. Herz, Acc. Chem. Res. 49 (2016) 146–154.
[40] T. S. Sherkar; C. Momblona; L. Gil-Escrig; J. Ávila; M. Sessolo; H. J. Bolink; L. J. A. Koster, ACS Energy Lett. 2 (2017) 1214-1222.
[41] W. Nandi; W. Yiliang; W. Daniel; S. Heping; D. The; G. Dale; B. Chog; F. Xiao; P. Jun; W. Thomas; C. Kylie; W. Klaus, Energy Technology 5 (2017) 1827-1835.
[42] S.-H. Turren-Cruz; M. Saliba; M. T. Mayer; H. Juarez-Santiesteban; X. Mathew; L. Nienhaus; W. Tress; M. P. Erodici; M.-J. Sher; M. G. Bawendi; M. Gratzel; A. Abate; A. Hagfeldt; J.-P. Correa-Baena, Energ. Environ. Sci. 11 (2018) 78-86.
[43] J. M. Ball; A. Petrozza, Nat. Energy 1 (2016) 16149.

[44] T. Leijtens; G. E. Eperon; A. J. Barker; G. Grancini; W. Zhang; J. M. Ball; A. R. S. Kandada; H. J. Snaith; A. Petrozza, Energ. Environ. Sci. 9 (2016) 3472-3481.
[45] F. Wang; S. Bai; W. Tress; A. Hagfeldt; F. Gao, npj Flexible Electronics 2 (2018) 22.
[46] D. Prochowicz; M. M. Tavakoli; A. Solanki; T. W. Goh; T. C. Sum; P. Yadav, J. Mater. Chem. C (2019).
[47] T. Matsui; J.-Y. Seo; M. Saliba; S. M. Zakeeruddin; M. Grätzel, Adv. Mater. 29 (2017) 1606258.
[48] A. Albadri; P. Yadav; M. Alotaibi; N. Arora; A. Alyamani; H. Albrithen; M. I. Dar; S. M. Zakeeruddin; M. Grätzel, J. Phys. Chem. C 121 (2017) 24903-24908.

Table 1: Summary of the different solar cell device parameters (planar-device configuration) measured under 1 Sun illumination.

Perovskite/ Parameters)	V_{OC} (V)	J_{SC} (mA-cm^{-2})	FF	PCE (%)	Series Resistance (ohm-cm^2)
MAFA	1.14	21.0	0.69	16.5	9
RbMAFA	1.15	22.2	0.67	17.1	7
CsMAFA	1.14	21.9	0.72	17.9	7
RbCsMAFA	1.17	22.4	0.73	19.1	5

Table 2: Summary of the recombination rate constants and electron and hole diffusion lengths for different perovskite films. PL kinetics obtained from 600 nm excitation wavelength at ~ 0.5 μJ-cm^{-2} pump fluence were used to estimate the charge carrier diffusion lengths in perovskite films.

Parameters/Perovskites	MAFA	RbMAFA	CsMAFA	RbCsMAFA
Monomolecular recombination (10^{-6} s^{-1})	10.0 ± 0.6	41 ± 1	24.7 ± 0.5	4.1 ± 0.6
Bimolecular recombination ($\times 10^{-11}$cm^3 ns^{-1})	0.79 ± 0.01	0.91 ± 03	1.01 ± 0.02	0.87 ± 0.01
Hole diffusion length (nm)	290 ± 10	290 ± 20	350 ± 20	460 ± 30
Electron diffusion length (nm)	510 ± 30	330 ± 20	610 ± 40	600 ± 40

Figures

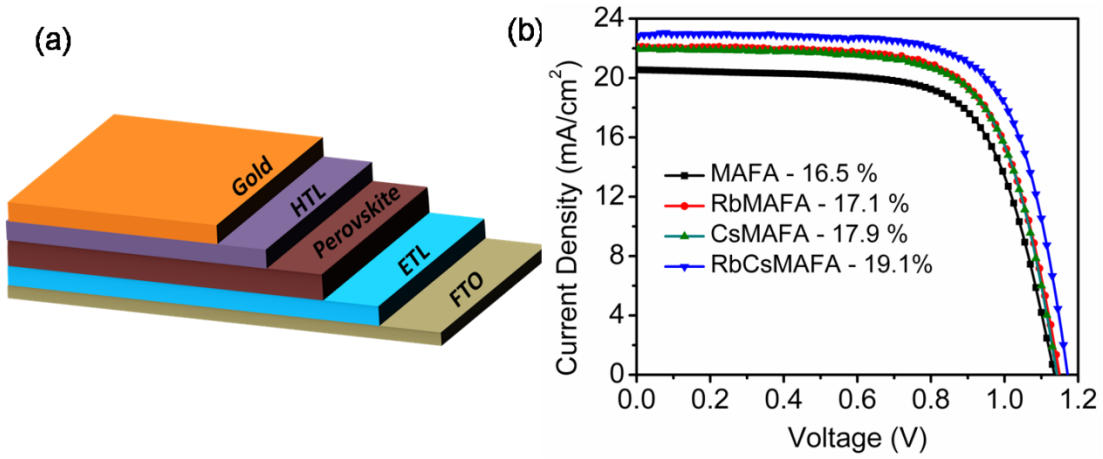

Figure 1. (a) Schematic of the device architecture, FTO/ETL(comp-TiO_2)/perovskite/HTL(spiro-OMeTAD)/Gold (b) light J-V characteristics of solar cell devices fabricated with perovskite films consisting different cations. The statistical PCE performance over 25 devices of each set is presented in figure S1.

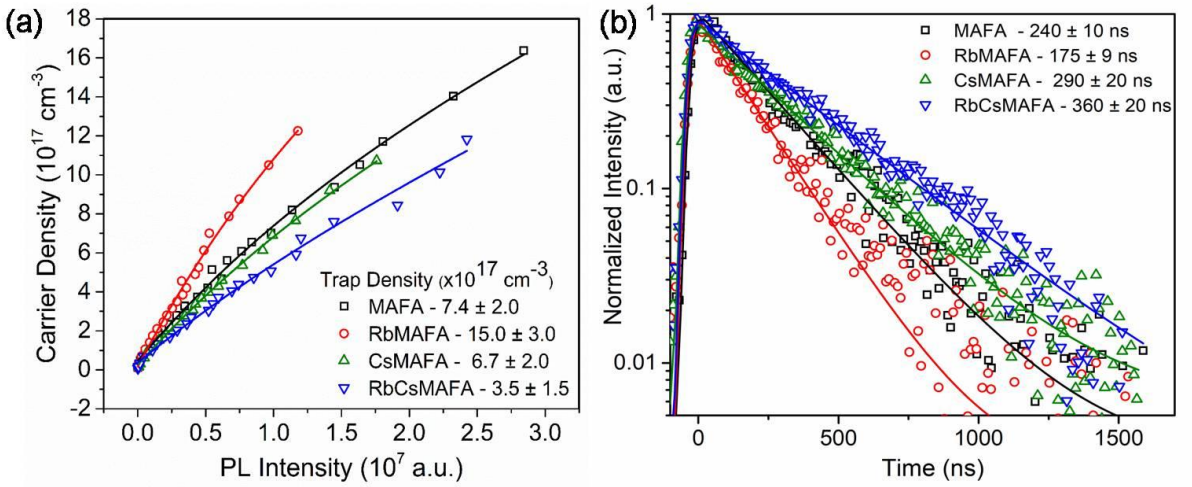

Figure 2. (a) Photoexcited carrier density as a function of integrated PL intensity of different perovskite films measured in the low fluence regime: solid lines are the corresponding fits of the experimental data with the trap density model, (b) mono-exponential fitting of low fluence PL kinetics. A pump wavelength at 600 nm was used to excite the samples.

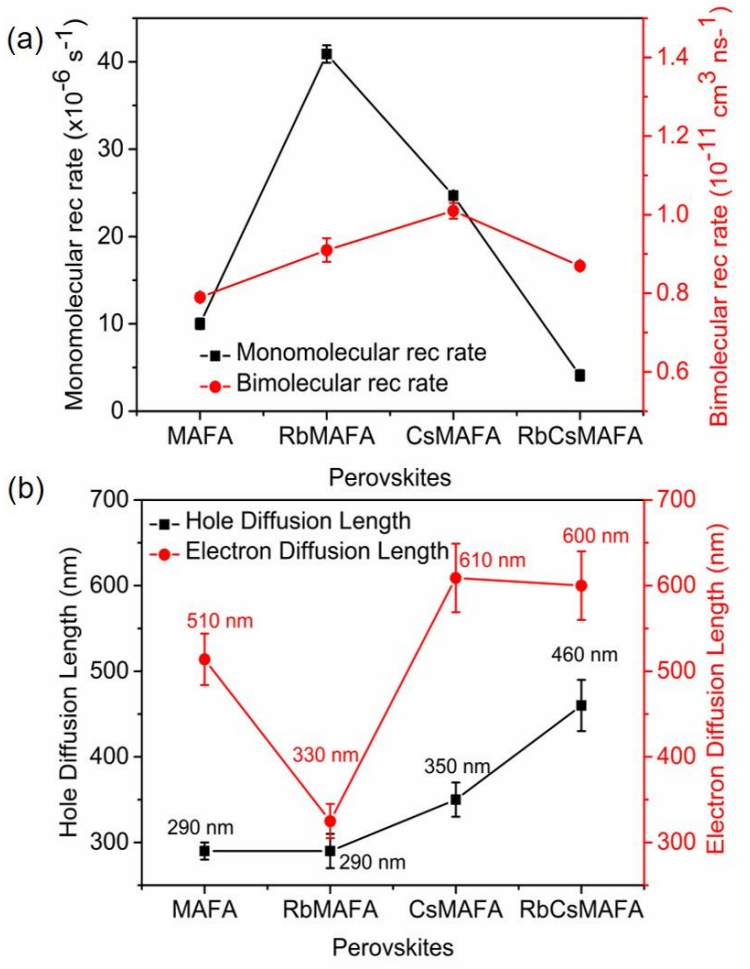

Figure 3. (a) Plots of monomolecular and bimolecular recombination rates and (b) represents the impact of different cations on electron and hole diffusion lengths in perovskite films. Refer to figure S5 and figure S6 for the fitting of the transient dynamics.

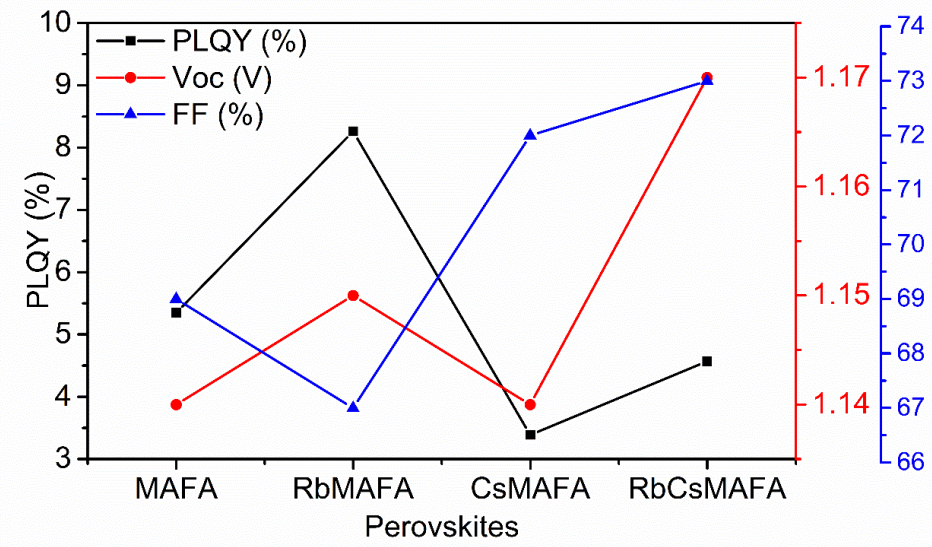

Figure 4. A plot of the variation of photoluminescence quantum yield (PLQY), V_{OC} and fill factor in relation to different cation-based perovskite films. PLQY was estimated by exciting different perovskite films by a 473 nm CW laser in an integrating sphere.

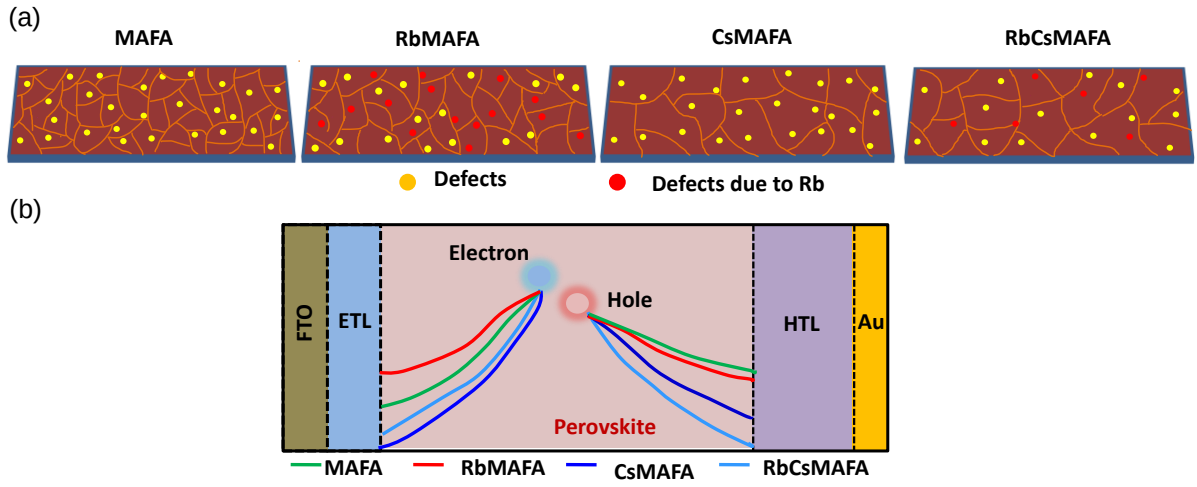

Figure 5. (a) Schematic illustration of the morphology and defects in different perovskite films. Grain boundaries, voids, non-perovskite phase etc. are the source of these defects which vary due to the interaction of different cations. (b) Schematic illustration of the relative electron and hole diffusion lengths in the different perovskite films (see Figure 3(b) for the actual values). The resulting diffusion length (electron and hole) in perovskite absorber layer is determined by a combined influence of defect density in absorber layer and extend of cation integration in perovskite crystal structure. Under illuminated conditions, the photo-generated charge carriers in RbMAFA perovskite layer suffer from limited electron and hole diffusion lengths, although it is sufficient to reach the respective electrodes in 400 nm thick perovskite film. On the other hand, an efficient charge collection probability in solar cell devices is expected for the increased

charge carrier diffusion lengths in CsMAFA. A more balanced carrier diffusion length in RbCsMAFA perovskites can also be expected.

TOC